Interstellar comet 2I/Borisov: dust composition from multiband photometry and modelling

Vladimir V. Busarev,[1,2]★ Elena V. Petrova,[3]★ Marina P. Shcherbina,[1] Natalia P. Ikonnikova,[1] Marina A. Burlak[1] and Alexander A. Belinski[1]

[1]*Lomonosov Moscow State University, Sternberg Astronomical Institute (SAI MSU), Universitetskii 13, Moscow 119992, Russia*
[2]*Institute of Astronomy, Russian Academy of Science, Pyatnitskaya 48, Moscow 109017, Russia*
[3]*Space Research Institute, Russian Academy of Sciences (IKI RAS), Profsoyuznaya 84/32, Moscow 117997, Russia*

ABSTRACT
We present results from multiband photometry of the interstellar comet 2I/Borisov (C/2019 Q4). The observations were carried out in the two months before its perihelion passage. The *UBVri* photometric data obtained for comet 2I were converted to its reflectance by means of observations of neighbouring solar analogues, which allowed the reflectance of the comet with wavelength to be calculated. The registered prominent changes in the reflectance spectra of 2I while it was approaching the Sun from 2.40 to 2.01 au, and numerical simulations of the light scattering by aggregate particles provide insight into the chemical-mineralogical and structural properties of the cometary dust particles. The close agreement between the trends observed in the spectral characteristics of 2I and some models suggests that, during the observations, conglomerates of magnesium-ferrous (and, probably, organic) submicron particles prevailed in the scattering by its matter, H_2O ice particles induced no noticeable spectral signals, and the gas contribution to the scattering by the coma was relatively small.

Key words: radiative transfer – scattering – instrumentation: photometers – methods: miscellaneous – techniques: spectroscopic – comets: individual: 2I/Borisov.

1 INTRODUCTION

Interstellar comet 2I/Borisov (provisional designation C/2019 Q4) was discovered in the morning of 2019 August 30 by Gennady Borisov, an amateur astronomer and an engineer at the Crimean Sternberg Astronomical Institute (SAI) Observatory of Lomonosov Moscow State University (MSU). He used a 65-cm telescope of his own design in these observations. It is interesting to note that this is the eighth comet discovered by Gennady Borisov, although he did not expect that it would be interstellar. After graduating from the Astronomical Department of the Faculty of Physics of MSU in 1984, Gennady did not become a professional astronomer, but retrained as a telescope engineer. Working at the Crimean observatory of SAI MSU, he personally assembled dozens of telescopes and, at the same time, conducted amateur observations with some of them. It was his avocation in astronomical observations that brought him worldwide fame.

Subsequent observations of comet C/2019 Q4 at other observatories made it possible to determine the hyperbolic shape of its extremely eccentric orbit, which became a clear indication of its interstellar origin. After that, the International Astronomical Union approved a new name for comet C/2019 Q4 – 2I/Borisov – as a second discovered interstellar object after 1I/'Oumuamua.

At the time of discovery, comet 2I already had a coma and a short dust tail; it was at a distance of 2.99 au from the Sun (approaching it at a speed of 40.5 km s^{-1}) and at a distance of 3.72 au from the Earth;

the value of its phase angle at that moment was 11°9. At first, the 2I nucleus size was estimated with insufficient accuracy (within 1.5–8 km) because of the large amount of dust in the coma (Bolin et al. 2020; Fitzsimmons et al. 2019; Jewitt & Luu 2019). The size of the cometary nucleus was determined more accurately, at ∼0.7 km, from *Hubble Space Telescope* photometric observations on 2019 October 12 (about a month before perihelion) and some model constraints (Jewitt et al. 2020).

In 2019, from the second half of September to early October, *UBVRI* observations of 2I were made with the 2.5-m Nordic Optical Telescope in the Canary Islands (Jewitt & Luu 2019). The measured colour indices of 2I, namely $E(B - V) = 0.80 \pm 0.05$, $E(V - R) = 0.47 \pm 0.03$ and $E(R - I) = 0.49 \pm 0.05$, characterize its dust matter and almost coincide with the average colour indices of long-period comets of the Solar system; they also turned out to be close to those of 1I/'Oumuamua (Jewitt & Luu 2019). It was also found that the colour indices of 1I and 2I are lower than the corresponding values for very red trans-Neptunian bodies, the colour of which is considered to be a sign of complex organics in their surface matter (Cruikshank et al. 1998; Jewitt & Luu 2019). This organic material can be formed at low temperatures (about several tens of degrees kelvin) under solar radiation exposure (Cruikshank et al. 1998). The absence of extremely red organics both in interstellar objects 1I and 2I and in atmosphereless bodies of the inner Solar system (Cruikshank et al. 1998; Jewitt 2002) may be explained by the influence of factors that prevent the occurrence or cause the decay of these compounds – relatively high temperature and hard radiation – as those bodies pass fairly close to the stars.

★ E-mail: busarev@sai.msu.ru (VVB); epetrova@iki.rssi.ru (EVP)

The first spectroscopic observations of the 2I comet revealed a strong cyanide emission band CN (0-0) at 3880 Å (Fitzsimmons et al. 2019), a Swann band of diatomic carbon (C_2) with a maximum at 5167 Å and a width of about 100 Å (at a level of $\sim 5\sigma$), and an oxygen forbidden line [O I] at 6300 Å (up to 5σ) (McKay et al. 2019). Given that the emission line of atomic oxygen is an indicator of emitted and dissociated H_2O in comets, the productivity of H_2O was calculated from the intensity of this line: $Q = (6.3 \pm 1.5) \times 10^{26}$ mol s^{-1} (McKay et al. 2019). Nevertheless, no spectral features of H_2O ice were detected in the 2I coma (Yang et al. 2020).

Similarly, the release rates of cyanide and diatomic carbon from the nucleus of 2I (within 1.6×10^{24}–6×10^{24} and 6×10^{23}–3×10^{24} mol s^{-1}, respectively) were obtained (McKay et al. 2019). A comparison of the listed values for 2I and comets of the Solar system showed that they are quite close, but 2I has a slightly higher $Q(CN)/Q(H_2O)$ and a significantly lower $Q(C_2)/Q(H_2O)$ ratio (Fitzsimmons et al. 2019; McKay et al. 2019; Opitom et al. 2019) than the averages for comets in the Solar system (A'Hearn et al. 1995; Cochran, Barker & Gray 2012). Thus, in terms of the gas release rates for C_2, CN and H_2O as 2I was approaching the Sun, 2I resembles the comets of our planetary system and is characterized as depleted in diatomic carbon.

In the above-mentioned papers about 2I and other comets, much attention was paid to the process of dust ejection from the nuclei and the properties of the dust particles themselves. From the model constraints on the physical parameters of dust particles and the length of the 2I dust tail as determined by the action of solar radiation pressure and gravitational acceleration, the speed of particle ejection from the cometary nucleus, the total volume of ejected dust, and the size of dust particles were estimated. In particular, a value of ~ 100 μm was found for the effective size of dust particles at a distance of 10^8 m from the 2I nucleus (at the end of the dust tail), while much larger values were obtained for the vicinity of the nucleus (Jewitt & Luu 2019; Cremonese et al. 2020). The properties of the 2I dust substance (e.g. Xing et al. 2020) were compared with the corresponding quantities of comet 67P/Churyumov−Gerasimenko, which was studied at great length during the implementation of the *Rosetta* space mission (ESA). It should be noted that the 2I colour index $E(R - I) = 0.49$ is very close to that of 67P (0.47), but their $E(V - R)$ colour indices differ, taking values of 0.47 and 0.53, respectively (Lamy & Toth 2009; Jewitt & Luu 2019). This means that the reflectance spectrum of 67P has a slightly higher gradient or is redder than that of 2I. As follows from the in situ analysis of the 67P dust composition with the Comet Mass Spectrometer of Secondary Ions (COSIMA) onboard *Rosetta*, the 67P dust particles are made of more than 50 per cent carbon and carbon-containing organic matter in mass (Bardyn et al. 2017). At the same time, laboratory simulations of the reflectance spectrum of the 67P nucleus showed that a large spectral gradient of the comet in the visible range may be most likely explained by the presence of hydrogen-rich macromolecular organics rather than by the high content of carbon (the reflectance spectrum of which has a low gradient) (Rousseau et al. 2018). Thus, the lower gradient of the spectrum of comet 2I in the visible range suggests that there is less organic matter of this kind in its composition as compared with 67P.

The above-mentioned estimates of the effective size of particles in the 2I coma (Jewitt & Luu 2019) are consistent with the dust particle parameters directly measured near the 67P nucleus with the GIADA, OSIRIS, MIRO and ROSINA instruments onboard the *Rosetta* spacecraft (Rotundi et al. 2015). These results were used to determine the total dust/gas ratio in the 67P matter; this ratio was estimated at ~ 4 by taking into account the contribution of large conglomerates (up to a metre in size), which separated from the cometary nucleus and moved around it, to the total dust mass (Rotundi et al. 2015). The obtained dust/volatile ratio may be considered as closest to the real values for the nuclei of 67P and similar comets, including 2I. Thus, for the first time, we have a chance to study the properties of alien dust matter.

In this paper, we analyse the results of the *UBVri* photometry of comet 2I and examine its dust composition from the spectral behaviour of its reflectance in the range of $0.38-0.73$ μm. We determine the span of changes in the spectra of 2I during its approach to perihelion (from 2.40 to 2.01 au to the Sun). Numerical simulations for the reflectance spectra of 2I, which exhibited a well-developed coma at the time of observations, allow us to gain insight into the sizes, structure and composition of submicron particles and their conglomerates in the 2I coma.

2 THE *UBVri* PHOTOMETRIC SYSTEM AND WAYS TO OPTIMIZE IT

In order to perform multiband photometric observations of comet 2I/Borisov, the RC600 (0.6-m) telescope at the Caucasus Mountain Observatory of SAI (SAI CMO) (at a height of 2112 m above sea level) was used. The telescope operates in semiautomatic mode and is equipped with an Andor (iKon-L DZ-936N-BV; 2048 × 2048 CCD; pixel size 13.5 μm) photometer with CCD cooling to $-60°$C (Berdnikov et al. 2020).

For observations of comet 2I, a combination of the Johnson *UBV* and SDSS *ri* light filters was used to achieve a more uniform coverage of the 0.30–0.85-μm spectral range than would be possible with the classical *UBVRI* system (e.g. Bessell 2005). Measurements of the filter spectral transmission (FST) were performed using an Avantes AvaSpec-2048 spectrophotometer. The FSTs of all filters and the quantum efficiency (QE) of the CCD matrix are shown in Fig. 1(a). Spectral bands of the combined 'CCD QE + *UBVri* FST' system (convolutions of the QE CCD and the measured *UBVri* FSTs), designated as U', B', V', r' and i', are shown in Fig. 1(b). Spectral bands of the entire photometric system, including the model spectral transmittance of the SAI CMO local atmosphere or the median atmosphere (MEDA) (see Fig. 1c), are convolutions of the $U'B'V'r'i'$ FSTs with the MEDA. These bands, designated as U'', B'', V'', r'' and i'', are presented in Fig. 1(d). The atmospheric spectral models were calculated with the LIBRADTRAN software package (Emde et al. 2016) by taking into account the physical parameters of the SAI CMO local atmosphere measured over several years (Kornilov et al. 2016a, 2016b) (Fig. 1b). As can be seen from a comparison of Figs 1(a) and (d), the CCD QE and spectral transparency of the local atmosphere induce almost no change in the effective wavelengths of the peaked *UBV* bands; however, they noticeably change the corresponding values for the rectangular *r* and *i* bands. Also, almost in the centre of the i'' band, at 761 nm (Fig. 1d), there is an intense telluric A-band of oxygen absorption of $O_2[X_0-b_0]$ (e.g. Kurucz 2005). Owing to the nearly flat shape of the r'' and i'' maxima, changes in the object brightness lead to larger errors in the effective wavelengths of these bands than in the corresponding values for the U'', B'' and V'' bands. The analysis of our photometric system yielded the following values for the effective wavelengths of the 'light filters + CCD-matrix + atmosphere' system (i.e. the U'', B'', V'', r'', and i'' bands) and their errors: 376 ± 1 nm (U''), 444 ± 1 nm (B''), 528 ± 1 nm (V''), 633 ± 13 nm (r''), and 723 ± 10 nm (i''). Thus, the errors in the effective r'' and i'' wavelengths turned out to be dependent on the object brightness – about an order of magnitude greater than those of the $U''B''V''$ bands. However, as will be shown below, these errors produce no significant effect on
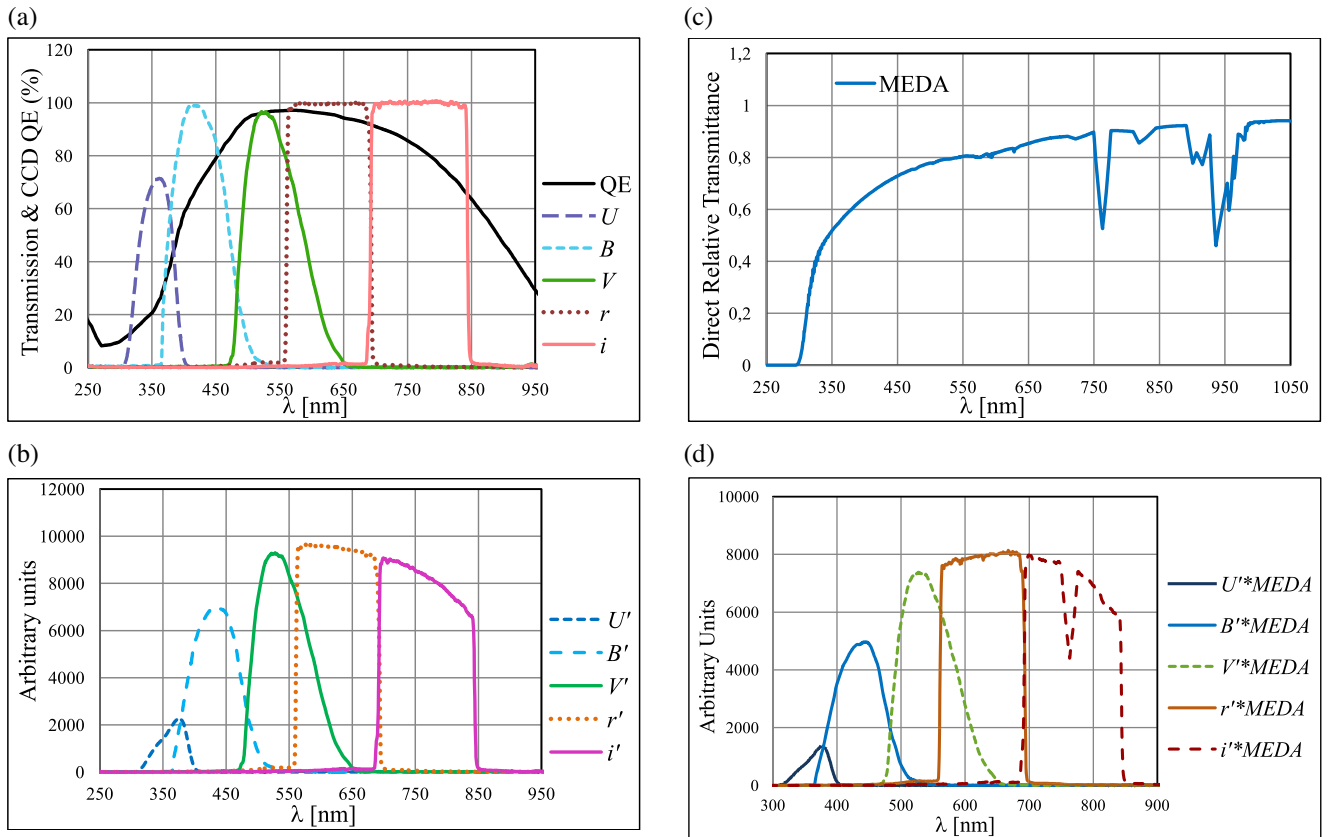
(a)

(c)

(b)

(d)

Figure 1. (a) The measured spectral transmissions of the *U*, *B*, *V*, *r* and *i* filters and the quantum efficiency (QE) of the CCD used. (b) Convolutions of the *UBVri* spectral transmission and CCD QE. The resulting curves are designated as *U′*, *B′*, *V′*, *r′* and *i′*. (c) The model direct transmittance of the terrestrial atmosphere at the SAI CMO location or the median atmosphere (MEDA for short) calculated with the LIBRADTRAN software package (Emde et al. 2016). (d) Convolutions of the *U′*, *B′*, *V′*, *r′* and *i′* bands with MEDA represent the *U″B″V″r″i″* photometric system used.

the results of the photometric measurements, nor on their modelling and interpretation, as the spectral features inherent in the 2I dust component are sufficiently broad.

Nevertheless, our experience of multiband observations of comet 2I and the data reduction prompted us to ask how the considered photometric system (or similar ones) may be optimized for a more effective performance with small 0.5-m telescopes and larger ones. As can be seen from Fig. 1(d), in order to avoid errors in the effective wavelengths of the *r″* and *i″* bands connected with variations of the object brightness, we should change the rectangular shape of the *r* and *i* light filters to triangular. Then, to exclude the influence of the intense telluric A-band of $O_2[X_0$-$b_0]$ on the *i″* band, the latter may be divided (by means of the corresponding light filters) into two subbands centred at 700 and 800−850 nm to leave the absorption band between them (Figs 1c and d). Similarly, an additional band of triangular shape may be used behind the series of telluric H_2O bands with a maximum at 950 nm (Fig. 1c and Kurucz 2005) to extend the spectral range up to 1000 nm.

3 MULTIBAND PHOTOMETRY OF COMET 2I

Our multiband photometry of comet 2I was performed in the two months before its perihelion passage, at heliocentric distances of ∼2.40–2.01 au. Simultaneously with the comet observations, non-variable solar-type stars were observed as solar analogues and standards for calculating the reflectance of 2I and determining the values of the spectral transparency function for the local terrestrial

atmosphere in each of the light filters. The dates, universal time of the observations, ephemerides, and other observational parameters of 2I, as well as the names of standard stars, are listed in Table 1.

The intensity of the light flux coming from comet 2I and standard stars was derived from the observational data with the MAXIMDL program. Before this, the data were primarily processed with standard procedures: the signal readout noise and dark currents were taken into account, the CCD flat field was corrected, and pulses from cosmic particles were removed from each of the frames. Then the reflectance of the comet at the effective wavelengths of the used photometric bands was obtained in the following way. For each of the observation sets, the intensities of light measured in the object (the comet or a solar analogue star) in the *U′*, *B′*, *r′* and *i′* bands were recalculated by taking into account the differences in the exposure time (if there was any difference) and the air mass during observations of the object in these bands relative to those in the *V″* band. Then the reflectance of 2I in each of the bands was calculated by dividing the intensity values obtained for the comet by that for the solar analogue star while accounting for the difference in the air masses.

Because comet 2I was a morning object, we did not have time to repeat measurements in each of the bands. So, here we present the individual spectral measurements of the intensity of light scattered by the comet. The relative statistical error of each of the measurements is not more than 3 per cent in the *U″* band and is less 1 per cent in the other bands. The accuracy and stability of the photometric system are confirmed by the small relative standard deviations in

Table 1. Observational data of comet 2I and standard solar-type stars.

UT date	Right ascension (h m s)	Declination (à '')	Geocentric distance (au)	Heliocentric distance (au)	Elongation (à)	Phase angle (à)	Magnitude (V)	Air mass	Standard solar-type star	Air mass
2019 Oct 10.082	09 43 11.00	+19 16 14.0	2.834	2.400	54.752	19.869	17.37	1.626	HIP46072	1.482
2019 Oct 18.076	09 57 50.36	+15 27 16.5	2.677	2.309	57.949	21.464	17.17	1.664	HIP46072	1.555
2019 Oct 28.069	10 15 58.81	+10 07 29.6	2.496	2.208	61.841	23.384	16.93	1.747	HIP46072	1.187
2019 Oct 29.077	10 17 47.80	+09 33 06.3	2.478	2.199	62.226	23.570	16.91	1.675	HIP46072	1.110
2019 Nov 04.075	10 28 33.46	+06 00 11.2	2.379	2.148	64.493	24.638	16.78	1.714	HIP46072	1.160
2019 Nov 10.092	10 39 15.37	+02 12 39.3	2.289	2.104	66.713	25.623	16.65	1.626	HIP46072	1.482
2019 Nov 15.090	10 48 04.18	-01 06 36.3	2.220	2.073	68.515	26.362	16.76	1.697	HIP46072	1.767
2019 Nov 18.087	10 53 19.29	-03 10 18.8	2.182	2.058	69.576	26.765	16.70	1.765	HIP46072	1.393
2019 Nov 19.104	10 55 05.85	-03 52 59.1	2.170	2.053	69.933	26.895	16.69	1.667	TYC 1189–1432-1	1.777
									HIP46072	1.915
2019 Dec 06.110	11 24 14.57	-16 26 44.8	2.010	2.007	75.658	28.403	16.48	2.104	HIP48272	2.221
2019 Dec 08.099	11 27 34.38	-17 58 18.6	1.997	2.007	76.296	28.492	16.46	2.257	HIP48272	2.115

Notes: (1) Standard exposure times for the comet were 900 and 600 s in filters *U* and *B*, respectively, and 300 s in the others. (2) Ephemerides of comet 2I were calculated with the IAU MPC Ephemeris Service of https://minorplanetcenter.net/iau/MPEph/MPEph.html.

the data obtained for the standard stars: these deviations are within 2−3 per cent in *U″* and *i″* bands and less 1 per cent in the other bands.

All reflectance curves derived from the data of our observations of 2I in 2019 are shown in Fig. 2. They are normalized to the reflectance value in the *V″* band, interpolated, and given with the observation dates. Each of the symbols (dots) on the interpolated reflectance curves presents the individual measurement of the intensity of light scattered by 2I in the corresponding photometric band, and the relative statistical errors of these measurements are within the sizes of the symbols. Note that, although the wavelength scale in Fig. 1 is expressed in nanometres (according to the presentation rules for characteristics of filters), we deliberately switch to microns in Fig. 2, to follow the presentation tradition existing for the reflectance spectra of small bodies.

4 MODELLING OF THE 2I REFLECTANCE SPECTRA

4.1 Definitions and modelling methodology

In theoretical simulations of the light-scattering phenomenon in cometary atmospheres, it is often assumed, especially in applications to polarimetry, that the concentration of cometary particles is low and the coma is optically thin, which allows the single-scattering characteristics calculated for cometary particles to be applied to the interpretation of observations. However, in the reflectance spectra of a comet, the distinct manifestation of spectral features depends on the number of scatterers in the medium. Moreover, the nucleus surface spectrum may reveal itself. Consequently, the intensity of light scattered by the system of the coma and the nucleus should be considered, and it is given as

$$I(-\mu, \varphi) = \mu_0 R_{11}(\mu, \mu_0, \varphi - \varphi_0)F_0. \tag{1}$$

Here (μ_0, φ_0) and $(-\mu, \varphi)$ specify the cosines of zenith angles of incidence and reflection μ_0 and μ, respectively, and the azimuths of the incident and reflected light φ_0 and φ, respectively; the incident sunlight is assumed to be unpolarized; πF_0 is the incident flux per unit area perpendicular to the incident beam; and R_{11} is the first element of the so-called reflection matrix of the medium (Hansen & Travis 1974; Mishchenko & Travis 1997). The latter is obtained with one of the radiative transfer procedures, which is usually applied to the plane-parallel model atmosphere above the underlying surface (see below).

To calculate the reflection matrix, it is necessary first to determine the elements of the single-scattering matrix of scatterers, which describes the changes in the angular distribution and polarization state of light singly scattered by particles in a layer (e.g. Hansen & Travis 1974; Mishchenko & Travis 1997). The first element, $F_{11}(\theta)$, of this matrix (where $\theta \in [0, \pi]$ is the angle between the incidence and scattering directions, i.e. $\theta = \pi - \alpha$, where α is the phase angle) characterizes the angular distribution of the scattered intensity; it is called the phase function and satisfies the normalization condition

$$\frac{1}{2} \int_0^\pi F_{11}(\theta) \sin\theta \, d\theta = 1. \tag{2}$$

The other quantities required for further modelling are the scattering, C_{sca}, and absorption, C_{abs}, cross-sections per particle. The single-scattering characteristics may be obtained with any computational method appropriate for the type of particles composing the examined medium. For this, the size, morphology and refractive index of scatterers should be specified. To describe the magnitude of the light
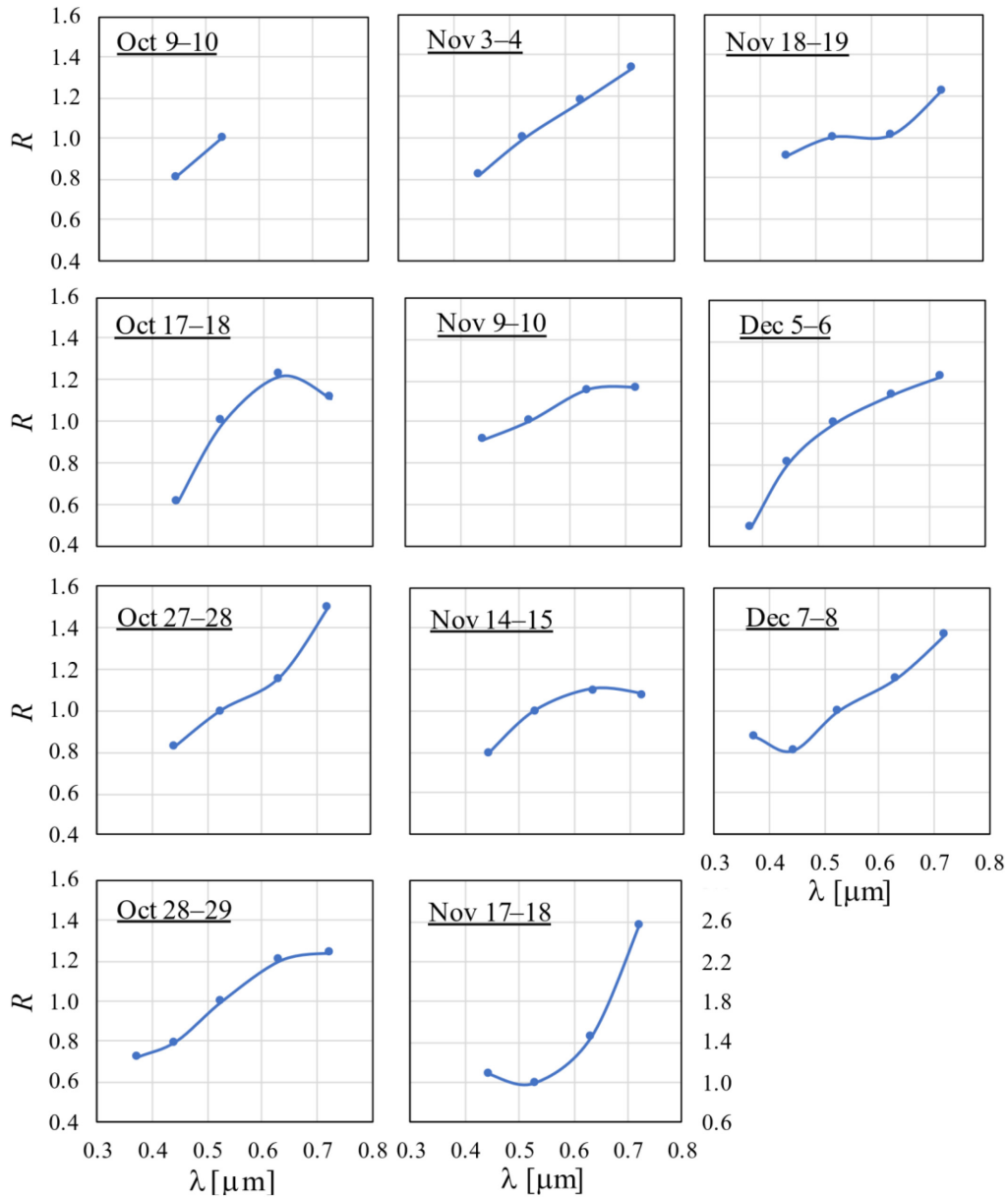
Figure 2. The spectral dependences of the reflectance R for comet 2I (nucleus + coma) observed in October−December of 2019 at heliocentric distances of 2.40 to 2.01 au. The diagrams are shown in chronological order from top to bottom in column order. The reflectance values measured at effective wavelengths of the $U''B''V''r''i''$ system (or $B''V''r''i''$, if the value in the U'' band is absent; on Oct 9–10, the measurements were made only in the B'' and V'' bands) are normalized to that at 0.528 μm and shown by symbols (dots), and the curves connecting them are polynomial interpolations. The relative statistical errors of individual measurements are within the sizes of the dots.

scattering in the atmosphere, the optical thickness is introduced as

$$\tau = \int_0^z k_{sca}\left(z'\right)dz', \qquad (3)$$

where z is the geometric thickness of the atmosphere counted from the upper boundary, and k_{sca} is the volume scattering coefficient of particles in each of the atmospheric layers, which is proportional to C_{sca}.

The underlying surface is regarded in the radiative-transfer procedure as a semi-infinite layer having certain reflection properties. In the simplest case, it can be assumed that the surface reflects light isotropically (according to Lambert's law), which means that the first element of the surface reflection matrix is the surface albedo.

4.2 Input parameters

4.2.1 Sizes and structure of particles

The results of both remote and in situ investigations of comets, which have been carried out most intensively over the last two decades, definitely point to the aggregate structure of cometary dust particles with submicron constituents (see e.g. Fulle et al. 2000; Kolokolova et al. 2004; Güttler et al. 2019; and references therein). Specifically, from the polarimetry of comets, it was found that the sizes of fragments and heterogeneities in the shape and/or composition of cometary dust particles are somewhat smaller than or comparable to the visible wavelengths; that is, the size parameter of constituent particles (CPs) in aggregates is $x \equiv 2\pi r/\lambda \approx 1.0-2.0$ (where r is

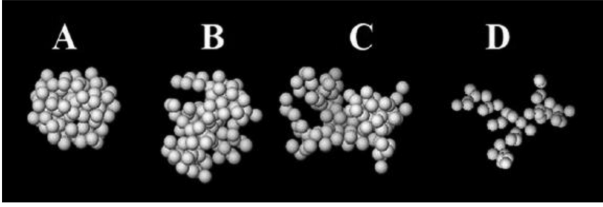**Figure 3.** The fractal-like aggregate structures considered.

Figure 4. The spectral dependence of the imaginary part of the refractive index of materials M3 and M4.

the CP radius and λ is the wavelength) (e.g. Petrova et al. 2000, 2004; Kimura et al. 2003; Lasue et al. 2009; Lumme & Penttilä 2011; Kolokolova et al. 2018; and references therein). Consequently, the electromagnetic interaction of the constituents should be taken into account in retrieving the properties of cometary dust from the results of optical observations in the visible range. To do this, model calculations of the light scattering by aggregates (clusters) are widely used (e.g. Tishkovets et al. 2004; Dlugach et al. 2011; Zubko et al. 2015; Kolokolova et al. 2018; Liu & Mishchenko 2018).

The morphology of cometary aggregate particles and its change while the particles are moving away from the nucleus are caused by disintegration owing to the evaporation of volatiles and agglomeration, which are intensified in the plasma environment of a comet (e.g. Ivlev et al. 2002; Dominik 2009). Based on a statistical fractal structure of cometary dust agglomerates (e.g. Mannel et al. 2016), we consider here fractal-like clusters. They are simulated with the diffusion-limited aggregation method (Mackowski 1995). The assumed fractal parameters are as follows: the pre-factor $k_f = 8$ and the fractal dimension $D_f = 3, 2.5$ and 2.1 (in the following, structures A, B and C) (see Fig. 3), which yield relatively densely packed structures; and $k_f = 5.8$ and $D_f = 1.9$ for a much fluffier structure D. The porosity of clusters p is determined from the so-called characteristic radius $R_c = (5/3)^{1/2} R_g$ (Kosaza et al. 1992), where R_g is the gyration radius of a cluster. Then, $p = 1 - N (r/R_c)^3$, where N is the number of CPs (monomers). For clusters A−D composed of 42 monomers with radii $r = 0.115$ μm (which corresponds to the mass-equivalent sphere with a radius $R_m = 0.4$ μm), $p = 0.54, 0.67, 0.78$ and 0.93, respectively.

It is worth stressing that our purpose here is to model the scattering properties of aggregate particles rather than the cometary particles themselves. Although the latter can be much larger than the structures considered here (see the Introduction), the positions of interference features produced by aggregates in the spectra become resistant to the growing of aggregates if the CP number has reached some value particular to a specified structure (see below). This allows us to consider rather small structures in the analysis of the spectral patterns characteristic of aggregate particles.

Although the aggregate structure with assumed fractal parameters and, consequently, the characteristics of the scattered light weakly but depend on realization peculiarities (Tishkovets et al. 2004), we consider here the spectra only for one of the structure realizations. The reason is that we are interested here only in the qualitative behaviour of the spectrum is its dependence on the cluster properties, and we do not average the modelled spectra over realizations to fit the measured one quantitatively.

The CPs in aggregates are assumed to be spherical in shape. This assumption is supported by two findings. First, as is seen from electron microscope images of interplanetary and cometary particles, the aggregate constituents are smooth in shape (e.g. Güttler et al. 2019; and references therein). Second, for aggregates composed of irregular particles, the scattering characteristics obtained from
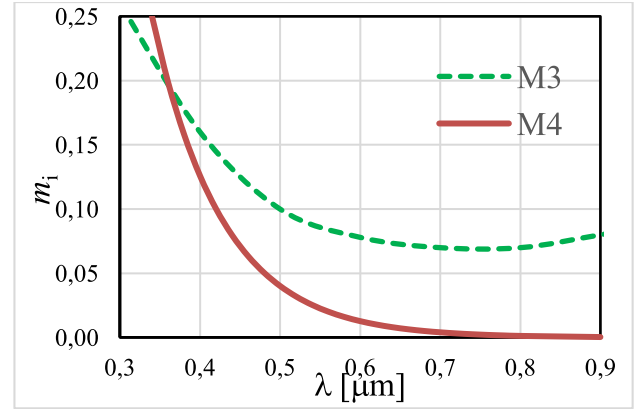
calculations (Xing & Hanner 1997; Lumme & Penttilä 2011; Zubko et al. 2015) and laboratory measurements (Gustafson & Kolokolova 1999) turned out to be close to those of multisphere aggregates, if the CP size parameters were small, $x < 2$. This is explained by some blurring out of the peculiarities in the scattering on individual spheres of these sizes by near-field effects if the CPs are close to each other in the aggregate.

Based on the above, in order to calculate the spectra of cometary dust aggregates, we choose three values for the CP radii: $r = 0.0955, 0.115$ and 0.130 μm. Several models were also calculated for clusters composed of CPs of different sizes. Although the smallest fragments identified in aggregate particles of the 67P coma are smaller than the CPs considered here (e.g. Güttler et al. 2019), the examination of spectra of structures with such small CPs would be of no practical interest for the present study, as the interference spectral features they produce are in the UV range, beyond the range considered here (see below). Consequently, our analysis does not exclude that the CPs of the considered sizes may contain even smaller heterogeneities.

4.2.2 Refractive index of particles

Because cometary dust particles are heterogeneous in composition and may contain both a dark (opaque) material and partially transparent silicates and volatile ices (e.g. Hanner & Bradley 2005; Bockelée-Morvan et al. 2017; Frattin et al. 2017), we consider four cases for the material of aggregates to analyse the effect of the dust composition on the spectrum shape.

(1) H_2O ice (hereafter, material M1): in the considered spectral range, the real part of the refractive index m_r changes slightly from 1.30 to 1.33 (Warren & Brandt 2008), while the imaginary part m_i is negligible and assumed to be 0.0.

(2) To show how a higher value of the wavelength-independent refractive index influences the spectrum shape, we consider a conventional material (M2) with $m_r = 1.80$ (which roughly corresponds to the mean value of m_r for Mg-Fe silicates) and $m_i = 0.10$.

(3) Mg-Fe silicate (olivine) (material M3) as one of the most abundant components of the cometary dust material: m_r varies from 1.78 to 1.81, while m_i decreases with increasing wavelength to ∼0.6 μm and further changes slightly (Dorschner et al. 1995) (Fig. 4).

(4) A mixture of different organic substances, which is collectively known in astronomy as tholins (material M4): although the refractive index of tholins essentially depends on the formation conditions, they generally exhibit a strongly increasing absorption in the short-

wavelength range, while m_r varies along the spectrum between 1.55 and 1.75 (e.g. West et al. 2014); in the present calculations, it is assumed that $m_r = 1.65$ and that m_i exponentially decreases with increasing wavelength (Fig. 4). The other organics considered as components of the cometary nucleus material, such as, for example, hydrogenated carbon, are close to M3 and M4 in terms of the refractive indices.

4.2.3 Coma optical thickness

In most of the models considered below, the optical thickness of the dust/ice coma is assumed to be $\tau = 0.5$ at $\lambda = 0.56 \ \mu$m; its change along the spectrum is accounted for according to the change in the scattering cross-section of the aggregates. To show the influence of τ on the reflectance spectra, the values $\tau = 0.1$ and 1.0 are tested in several models.

To analyse the effect of the gaseous component on the coma reflectance spectrum, the models for homogeneously mixed dust/ice particles with gas are calculated. It is assumed that the gas optical thickness is $\tau_{gas} = 0.01$ at 0.56 μm and changes along the spectrum according to Rayleigh's law, $\tau_{gas} \sim 1/\lambda^4$.

4.2.4 Underlying surface

Most comets display dust activity at heliocentric distances of ~ 4 au and less, where dust can be detached from the nucleus by water gas pressure at a temperature $T > 205$ K (Cremonese et al. 2020; Fulle et al. 2020). Consequently, in these comets, a noticeable coma develops, and the dust component contribution absolutely dominates the reflectance spectra. However, when modelling the reflectance spectra, we should also test the case of an optically thin coma, which means that the spectral characteristics of the nucleus may reveal themselves in the spectra. Because the true shape of the 2I nucleus spectrum is unknown and the investigated nuclei of near-Sun comets are reddish and very dark (e.g. Capaccioni et al. 2015) and resemble D-type asteroids (Fitzsimmons et al. 1994), we take the reflectance spectra of two asteroids, namely 152 Atala (D-S type) (Bus & Binzel 2003) and 624 Hektor (D type) (Vilas et al. 1998), as examples for the spectrum of the 2I nucleus. Their spectra are different in shape and show essentially positive gradients typical of D-type asteroids (Fig. 5). We also take into account that the Tagish Lake meteorite, which is considered to be a fragment of a D-type asteroid (Hiroi et al. 2001), exhibits a much broader variety of organic materials than frequently occurring carbonaceous chondrites (Pizzarello et al. 2001). It should be emphasized that, although Atala is apparently an asteroid of the intermediate D-S type (Tholen 1989; Bus & Binzel 2002), in simulations we use only the shape of its reflectance spectrum to test its effect on the 2I model spectrum. The spectra of the nucleus of comet 67P measured in the VIRTIS/*Rosetta* experiment also exhibit a positive gradient in the range 0.5−0.8 μm, as do the mentioned asteroids, but varying from area to area over the nucleus (Filacchione et al. 2016).

Moreover, when calculating the light-scattering models for the spectral range of the considered observations, we have to extrapolate the spectra of asteroids Atala and Hektor to $\lambda < 0.4 \ \mu$m. We take different spectral gradients in order to reveal the influence of the nucleus reflectance properties on the cometary spectrum at short wavelengths. In calculations we mainly use the Atala spectrum extrapolated to short wavelengths (Fig. 5, orange dashed curve). Its gradient is not extremely steep and takes intermediate
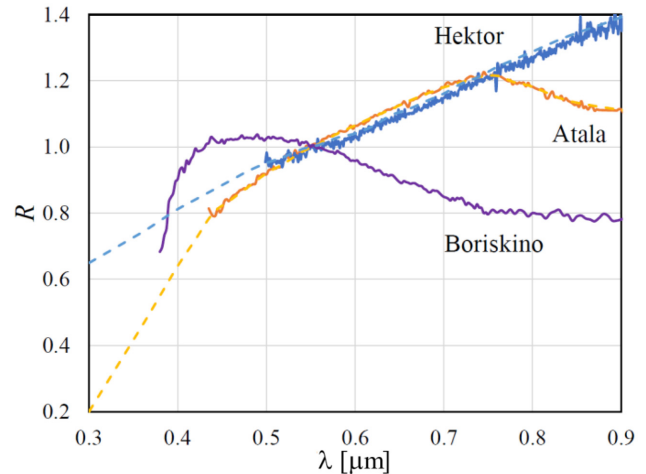

Figure 5. The spectral dependence of the reflectance R (normalized to that at $\lambda = 0.55 \ \mu$m) of asteroids 152 Atala and 624 Hektor and the CM2 Boriskino meteorite (solid curves), and the approximation for asteroids extrapolated to short wavelengths (dashed curves) for model calculations.

values between those for Hektor and Boriskino CM2 carbonaceous chondrite (Busarev et al. 2002). The albedo of the 2I nucleus surface was assumed to be 0.05 at $\lambda = 0.55 \ \mu$m.

4.3 Computational techniques

At present, one of the most versatile and efficient direct computer solvers of the macroscopic Maxwell equations widely applied to the computation of electromagnetic scattering by an arbitrary multisphere configuration is the numerically exact superposition T-matrix method (Mackowski & Mishchenko 1996; Mishchenko et al. 2002). Consequently, we use the corresponding publicly available FORTRAN code (Mackowski & Mishchenko 2011) to compute the elements of the single-scattering Stokes matrix and cross-sections for the generated clusters in random orientation.

Then, the resulting single-scattering characteristics of clusters are used to compute the intensity of light scattered by the coma−nucleus system. Because our task is to interpret the results of integral measurements, we may assume that (i) the nucleus surface scatters light isotropically, which makes the computations substantially easier, and (ii) the coma is homogeneous and the properties of cometary dust do not change with distance from the nucleus. We use the radiative transfer procedure based on the invariant imbedding technique described in detail by Mishchenko & Travis (1997, and references therein).

Because this procedure deals with plane-parallel atmospheric layers, we calculated the intensity of scattered radiation for small areas of a sphere approximating the coma around the nucleus. The intensity values obtained for these areas (roughly $3° \times 3°$ in latitude and longitude), within which the scattering medium is considered as plane-parallel, were integrated over the sphere, accounting for the most frequent phase angle in the considered observations of 2I, which ranged from $19°.9$ to $28°.5$. It is immediately worth noting that variations of the phase angle within $\pm 15°$ weakly influence the shape of the model spectra, as the single-scattering phase functions of the considered aggregates show no strong features in the backscattering domain at each of the wave-lengths.
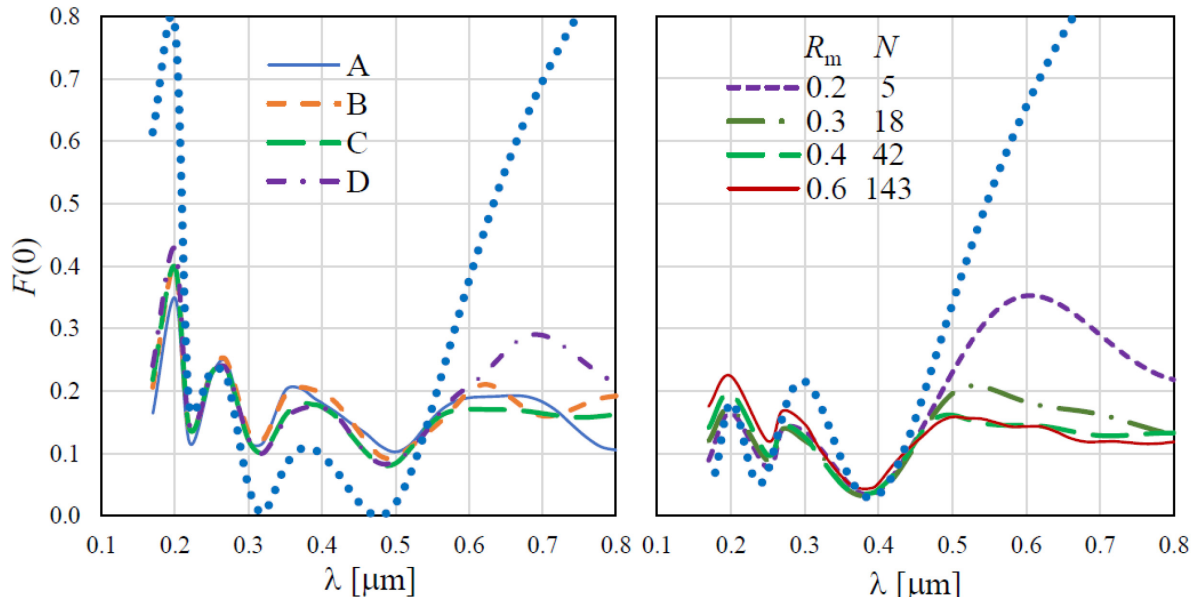
Figure 6. (Left) The single-scattering phase function in the backscattering direction $F(0)$ as a function of wavelengthfor aggregates of different structures are compared with that of individual spherical particles composing these aggregates (material M2); the number of CPs in aggregates is $N = 42$, and their radius is $r = 0.115$ μm. (Right) The change in the wavelength dependence of $F(0)$ for aggregates of structure C with increasing CP number ($r = 0.115$ μm, material M1); the curve for single CPs of these aggregates is shown (dotted) for comparison. In all of the models, the assumed wavelength step is 0.02 μm. R_{m} is the radius (in microns) of a mass-equivalent sphere for these aggregates.

4.4 Spectra of aggregates in the backscattering domain

A recent analysis of the visible spectra of light scattered by aggregate particles with submicron constituents to the backward hemisphere revealed the peculiarities that distinguish these spectra from those of homogeneous particles (Tishkovets & Petrova 2020). For aggregates with a spectral-independent refractive index and size R_{m}, the scattering cross-section C_{sca} gradually increases with decreasing λ and then forms a gently sloping hump at λ corresponding to $X_{\mathrm{m}} = 2\pi R_{\mathrm{m}}/\lambda \approx 10$ for ice CPs, while for homogeneous ice spheres this hump is at $x \approx 6$. Hence, the wavelength dependence of C_{sca} may not introduce any strongly pronounced features into the reflectance spectra. The changes in the shape of the phase function in dependence on λ are more complicated and show different trends in different phase intervals. Because our task is to analyse the reflectance spectra of the comet, we focus here on the spectral behaviour of the phase function in the backscattering direction, at $\alpha = 0°$, namely $F(0)$ (the subscripts are omitted for simplicity).

Examples of spectral curves for aggregates of different structures and aggregates containing a different number of CPs are shown in Fig. 6 in comparison to the dependences for single spherical particles (the dotted curves) that compose these aggregates. As is seen from the diagrams, the interference features induced by scattering on individual CPs survive in the spectra of their aggregates. At the same time, instead of the continuously growing $F(0)$ of single particles at longer wavelengths, where they become much smaller than the wavelength and scatter light more isotropically, their aggregates exhibit a maximum (at $\lambda > 0.5$ μm), which is caused by the interference of waves singly scattered by different CPs in the aggregate (Tishkovets & Petrova 2020).

The positions of the 'individual' extrema, as well as that of the 'collective' maximum, depend on the sizes of CPs in the aggregate and the real part of their refractive index: the entire interference

pattern moves to longer wavelengths as these parameters increase. This means that, for aggregates with CPs twice as small as those presented in Fig. 6 (e.g. corresponding to the smallest identified fragments in the 67P coma particles), the collective maximum would have been at $\lambda = 0.25-0.30$ μm, beyond the spectral range of the considered observations.

The shape and position of the collective maximum also depend on the number of CPs N in the cluster and its structure. However, this is true only if N is not large enough: the collective maximum moves to shorter wavelengths, to the first individual minimum (at $\sim$0.5 and $\sim$0.4 μm in the left-hand and right-hand panels, respectively), when N increases to some value, after which this maximum becomes resistant to the further growth of the cluster (at $\sim$0.6 and $\sim$0.5 μm in the left-hand and right-hand panels, respectively), because a further increase of N in a specified structure does not involve new effective participants in the interference of waves scattered by different CPs (for more details, see Tishkovets & Petrova 2020). This property of the spectral features produced by aggregates allows us to consider ensembles of rather small sizes to simulate numerically the reflectance spectra of the cometary dust.

The fluffier the cluster, the more CPs are required for the collective maximum to reach a stable position in the spectrum. For example, in the left-hand panel, the maximum for structure D containing 42 CPs is at $\sim$0.7 μm; and as this structure grows, it will move to $\sim$0.6 μm, where the collective maxima of more densely packed aggregates with $N = 42$ are located. Consequently, relatively small fluffy clusters may produce a rather high collective maximum at longer wavelengths than densely packed ones with CPs of the same size and material. If aggregates contain CPs of varying sizes, the collective maximum still survives, while the extrema induced by scattering on individual CPs are naturally smoothed (see below).
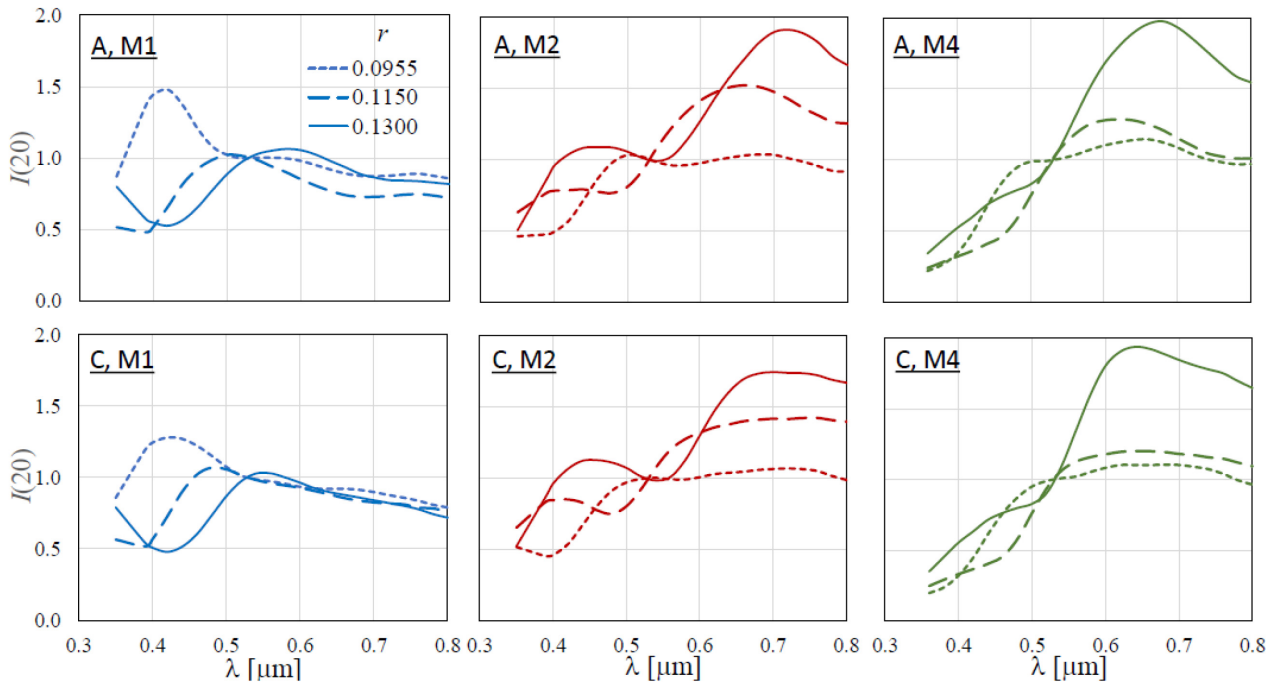
Figure 7. The spectra of the intensity of light scattered by the coma−nucleus system at the phase angle $\alpha = 20°$, $I(20)$, normalized to the value at $\lambda = 0.53$ μm. Each of the diagrams contains the spectral curves for three specified radii of CPs in the aggregates of structures A (upper row) and C (lower row). Three cases of the material (specified in the plots) are presented. The optical thickness of the coma is assumed to be $\tau = 0.5$. The spectrum of the underlying surface is assumed to be that of the asteroid Atala.

4.5 Model spectra of the coma–nucleus system

Let us now trace how the trends in the spectra of aggregates as functions of their properties may reveal themselves in the spectrum of a cometary coma composed of aggregates. In the models presented below (except Figs 10 and 11), it is assumed that the optical thickness of the coma is 0.5, the spectral properties of the underlying nucleus surface correspond to those of the asteroid Atala, and the surface albedo is $A_s = 0.05$ at $\lambda = 0.55$ μm. We show the calculated spectral curves of the intensity for $\alpha = 20°$ normalized to the value at $\lambda = 0.53$ μm, as in the measured spectral profiles.

The model profiles for three sizes of CPs in two aggregate structures (with $N = 42$) and three types of materials are shown in Fig. 7. It is seen that the curves for the coma containing ice clusters with 0.115-μm CPs (Fig. 7, left-hand column) definitely follow the single-scattering spectra of the composing clusters, and the collective maximum at ∼0.5 μm and the first individual minimum near 0.4 μm survive the multiple scattering (compare with Fig. 6, right-hand panel). In the spectra of the coma containing clusters with smaller or larger CPs, these interference features are naturally shifted to shorter or longer wavelengths, respectively. The increase in the real part of the refractive index (material M2; Fig. 7, central column) expectedly moves these features to longer wavelengths (compare with Fig. 6, left-hand panel), and the absorption, increasing at short wavelengths (material M4; Fig. 7, right-hand column), suppresses the details in this range. A comparison of the profiles for structures A and C (Fig. 7, upper and lower rows) shows that the structure variations produce a weak effect on the interference feature positions, while they may influence the strength of these features. This is also clearly seen in the left-hand panel of Fig. 8, where the profiles for four structures are compared. A relatively low sensitivity of the spectral profiles to the sizes of the considered clusters (or the number of CPs) is evident from the

right-hand panel of Fig. 8: only the shape of the long-wavelength slope of the collective maximum noticeably varies as the clusters grow.

The influence of the differing sizes of CPs in clusters on the spectrum of the coma was examined by an example of structures constructed in the following way. Because such clusters cannot be built with fractal relationships, we randomly filled a specified volume with spherical particles randomly varying in size within $d = \pm 10$ per cent around the assumed mean value. The number of CPs and the packing density were specified according to the values for a rather densely packed cluster of structure A. We used the volume of a slightly 'distorted' sphere, as structure A is more or less equidimensional, but we tried to avoid the wavy spectral features induced by scattering on a large spherical particle. The size of the filled 'quasi-sphere' was varied until the required packing density of the polydisperse cluster was obtained. Then, the same volume was filled up with spherical particles with sizes differing within a range of $d = \pm 20$ per cent, which resulted in a somewhat smaller packing density of CPs in the cluster.

As may be expected, the larger the variations in the CP sizes, the more effectively 'individual' short-wavelength features are smoothed (Fig. 9). At the same time, the collective maximum at longer wavelengths ($\lambda \approx 0.60-0.75$ μm for the considered CP sizes and material M2) survives.

Thus, as is seen from the comparison of Fig. 6 with Figs 7−9, if the optical thickness of the coma is $\tau = 0.5$, the features observed in the single-scattering spectra of aggregates, composing the coma, definitely reveal themselves in the spectra of the intensity of light scattered by the coma−nucleus system. Naturally, these features become more pronounced in the spectrum for higher values of τ, while the nucleus surface spectrum is mostly observed if the coma is thin (Fig. 10). However, even for $\tau = 0.5$, the nucleus surface
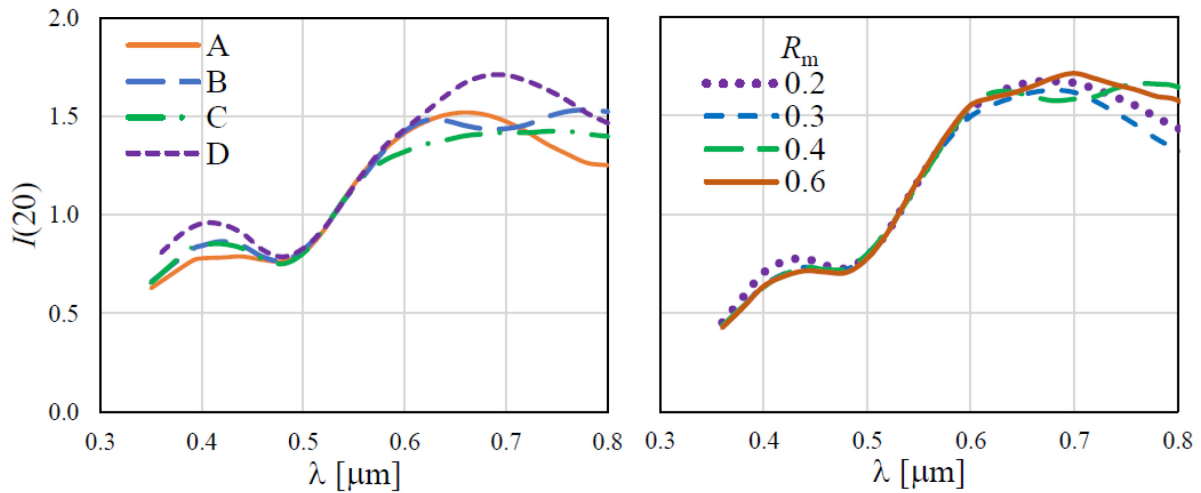
Figure 8. (Left) The spectra of $I(20)$ for different aggregate structures are compared, for $N = 42$, $r = 0.115 \, \mu$m, and material M2. (Right) The spectra of $I(20)$ for aggregates with increasing CP number N are compared: structure B, $r = 0.115 \, \mu$m, and material M3. R_m is the radius (in microns) of a mass-equivalent sphere for these aggregates.
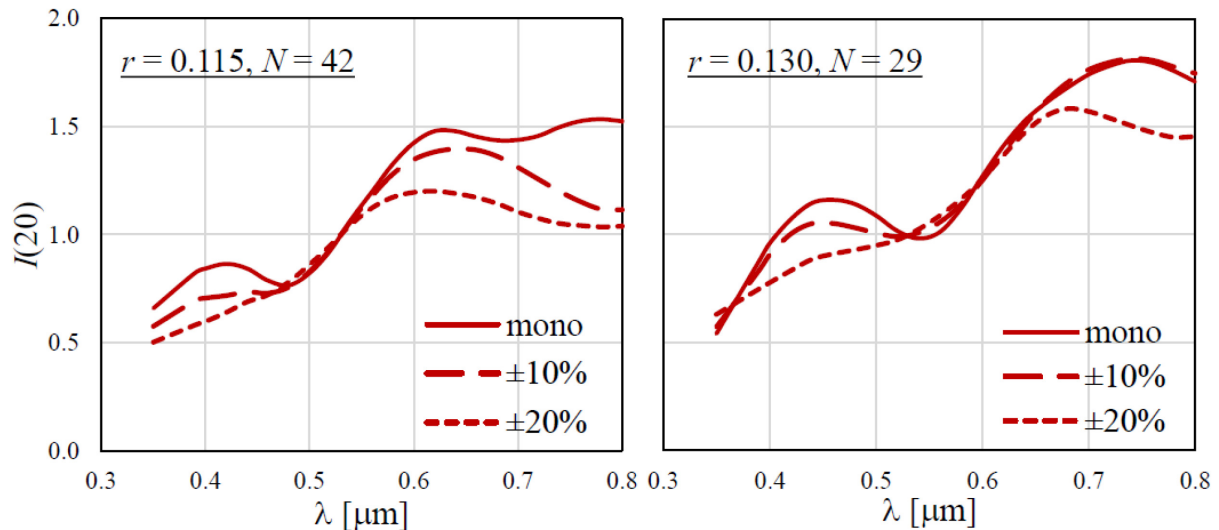

Figure 9. The spectra of $I(20)$ for clusters containing particles of different sizes with the deviation d from the mean radii $r = 0.115 \, \mu$m (left-hand panel) and $r = 0.130 \, \mu$m (right-hand panel). The CP number is 42 and 29, respectively, which corresponds to $R_m = 0.4 \, \mu$m, structure B, and material M2. Curves for aggregates containing particles of the same size are shown for comparison.

properties may produce a noticeable effect on the spectra for the coma−nucleus systems (Fig. 11, left-hand panel).

It is evident that the gas component of the coma may reveal itself by increasing the intensity at short wavelengths, which may even change the positive spectral gradient of the spectrum to a negative one in this range (Fig. 11, right-hand panel). The same effect may be expected from homogeneous particles that are much smaller than the wavelength in size.

5 DISCUSSION AND CONCLUDING REMARKS

The reflectance spectra of asteroids and other atmosphereless celestial bodies in a range from the near-UV to near-IR contain mineralogical absorption bands, which makes it possible to analyse the composition of their material from remote spectrophotometric measurements (e.g. McCord et al. 1970; Gaffey et al. 1989). However, as follows from the results of the present modelling, in

studies of comets with a well-developed coma (including 2I) by this method, it is necessary to take into account one more factor: the observed reflectance spectrum may contain wide maxima and minima caused by the light scattering on aggregates of submicron dust/ice particles with various refractive indices. At the same time, in the integral reflectance spectrum of comets with a developed coma ($\tau \geq 0.5$), the formation of distinct mineralogical absorption bands, like those for asteroids, seems unreal. Because the coma particles are in constant motion, the selective spectral absorption of light is washed away by different ensembles of particles with similar optical parameters.

Moreover, it should be stressed that spectral changes of the interpolated reflectance spectra of 2I (Fig. 2) are spaced by time intervals of 1 to 16 d, which corresponds to many rotations of the cometary nucleus, from several turns to dozens of turns, under the assumption that the rotation period of 2I is near the mean value for cometary nuclei, $\sim$15 h (e.g. Whipple 1982). Consequently, the
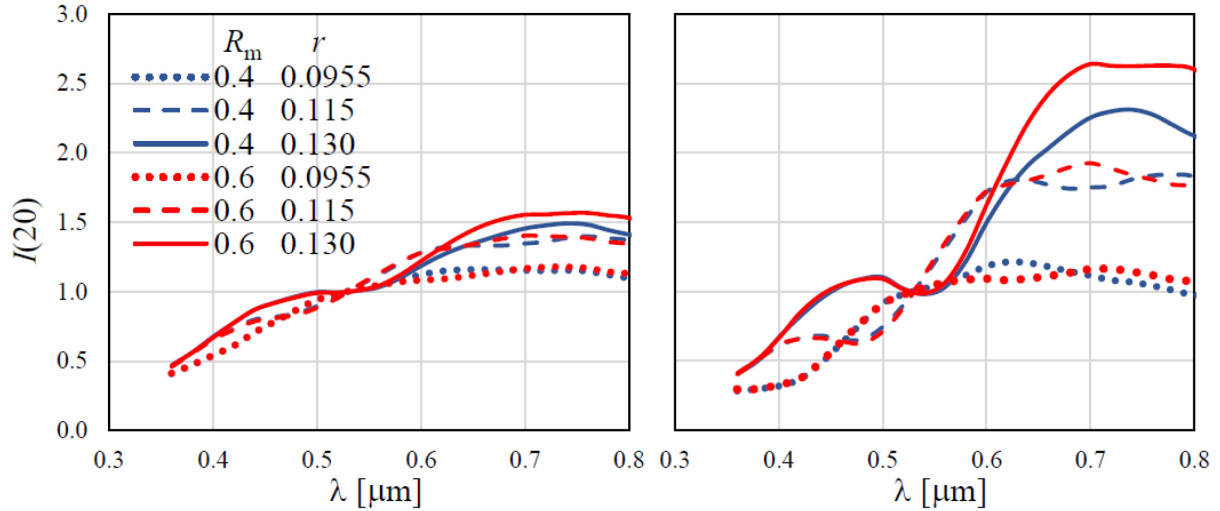
Figure 10. Influence of the optical thickness of the coma on the spectra of $I(20)$: $\tau = 0.1$ (left-hand panel) and $\tau = 1.0$ (right-hand panel) at $\lambda = 0.56$ μm. Examples for two values of R_m and three values of r are shown; structure B and material M2. R_m is the radius (in microns) of the mass-equivalent sphere for these aggregates.
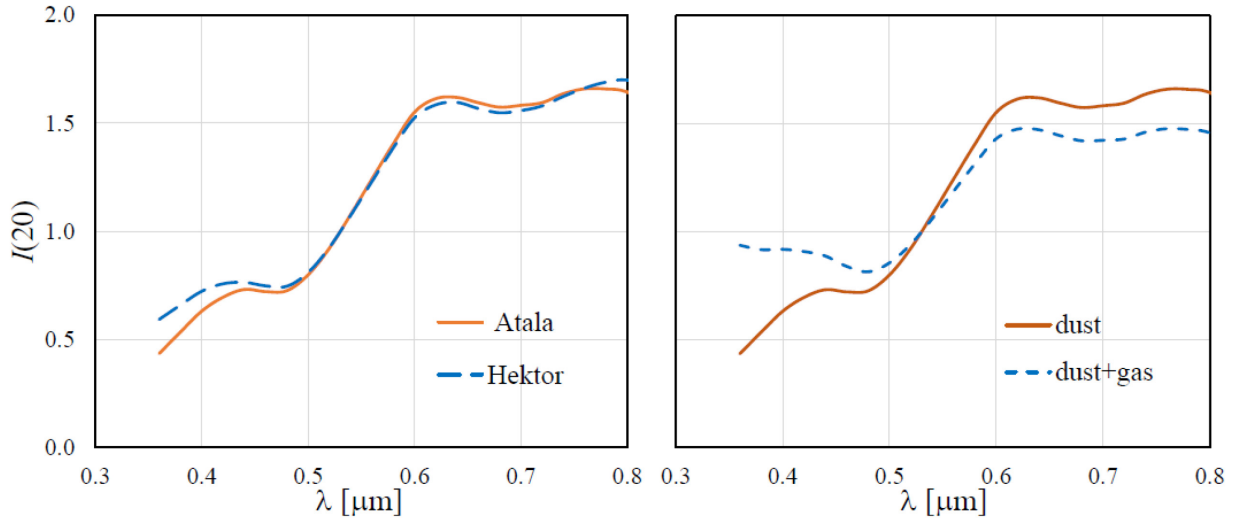

Figure 11. (Left) Spectra of $I(20)$ for different spectral properties of the underlying surface, corresponding to those of asteroids Atala and Hektor. (Right) Influence of the gas contribution on the spectra of $I(20)$; the gas optical thickness is $\tau_g = 0.01$ at 0.56 μm. In all models, the coma optical thickness is $\tau = 0.5$ at 0.56 μm, and the aggregate properties are: $R_m = 0.4$ μm, $r = 0.115$ μm, structure B, and material M3.

dust/ice particles leaving the nucleus have enough time to fill the observed coma. At the same time, in spite of the fact that, judging by the measurements of the 67P coma, the velocity of dust particles is rather low (mainly a few metres per second) (Rotundi et al. 2015), the possible presence of gas-dust jets, rotating with the nucleus and changing the orientation (e.g. Tenishev et al. 2016), may accelerate variations in the spectral features of the dust. For these reasons, we assume the changes measured in the spectra of 2I to be representative of changes in the properties of particles in its coma. (However, it is worthwhile to note that rotating jets were not directly observed in 67P.)

Thus, from a comparison of the modelled integral reflectance spectra with those of comet 2I (observed at heliocentric distances of $\sim 2.50 - 2.01$ au), the following properties of the 2I coma particulate material can be inferred.

(1) No signs of very small H_2O ice particles or their aggregates were found, because no negative spectral gradient and/or no characteristic maximum at 0.4 μm (as in Fig. 7, left) is observed in the interpolated reflectance curves of 2I in Fig. 2. However, aggregates of larger ice constituents cannot be excluded from probable scatterers in the coma, because they may contribute to the 'collective' maximum observed at longer wavelengths.

(2) Dust particles containing Mg-Fe silicates and tholins definitely prevail in the light scattering by the 2I coma, which follows from the positive gradient in the entire spectral range considered, including the substantial growth in the intensity at $\lambda > 0.6$ μm.

(3) In some measured spectra (Fig. 2, plots for Nov 17−18 and Dec 7−8), the intensity starts to increase towards short wavelengths; or its decrease becomes less steep (as for Oct 28−29). This points to the Rayleigh scattering strengthening and indicates the intense

release of gaseous compounds (H_2O and others) from the 2I nucleus (see also Section 1). The sporadic character of this release may be associated with the inhomogeneous distribution of active areas on the 2I nucleus and its rotation. The shape of the curve for Nov 17−18 is most representative: it exhibits not only a noticeable increase at short wavelengths, which is expectedly caused by the strengthening of Rayleigh scattering, but also pronounced growth at the long-wavelength end of the range. The latter may be induced by a substantial amount of relatively coarse-grained dust aggregate particles ejected into the coma by gas flows. Consequently, the changes in the reflectance along the wavelength measured on Nov 17−18 can be considered to correspond to the most active area of the 2I nucleus surface.

(4) The convex shape of three spectra exhibiting a maximum at 0.63 μm (for Oct 17−18 and Nov 14−15) characterizes a quieter state of the cometary coma. This is confirmed by a very low level of the signal in the *U* band, which could not even be registered for the standard exposure time on those nights. Consequently, this suggests that the Rayleigh scattering is not noticeable and the flux of gases released by the nucleus is relatively weak. This spectrum shape is closest to the model spectra for Mg-Fe silicates in Fig. 8 (right-hand panel), which is consistent with inference (2) of this list.

(5) Even for the coma optical thickness $\tau = 0.1$, the model reflectance spectrum of the coma−nucleus system differs from that of the nucleus surface and contains weak features induced by scattering on aggregates in the coma. This confirms the importance of the spectral characteristics of coma particles for the integral spectrum of the comet.

(6) Thus, numerical simulations of the spectral characteristics of comet 2I with a developed coma have shown that the light scattering on coma particles plays an important role in the formation of the spectrum of the comet in the range of ∼0.35−0.80 μm. Based on this modelling, the considerable predominance of the Mg-Fe and organic dust component in the coma of comet 2I has been determined. This conclusion is consistent with the results of direct measurements of the structure and composition of the dust material (including the general estimate of the dust-to-volatiles ratio) of comet 67P/Churyumov−Gerasimenko (see Section 1), which resembles 2I in the visible-range colour indices.

(7) As the present multiband photometry analysis and other spectral investigations (see Section 1) of interstellar comet 2I/Borisov show, this comet resembles 67P/Churyumov−Gerasimenko and other comets of the Solar system in the structure and composition of the coma particulate matter. This suggests that, in different planetary systems, cometary nuclei were formed under similar conditions and by similar mechanisms.

DATA AVAILABILITY

The source files for all figures in this paper (with the exception of Fig. 3 including an image) are available on the reference http://lnfm1.sai.msu.ru/~busarev/.

REFERENCES

A'Hearn M. F., Millis R. C., Schleicher D. G., Osip D. J., Birch P. V., 1995, Icarus, 118, 223
Bardyn A. et al., 2017, MNRAS, 469, S712
Berdnikov L. N. et al., 2020, Astron. Rep., 64, 310
Bessell M. S., 2005, ARA&A, 43, 293
Bockelée-Morvan D. et al., 2017, MNRAS, 469, S443
Bolin B. T. et al., 2020, AJ, 160, 26
Bus S., Binzel R. P., 2002, Icarus, 158, 146
Bus S., Binzel R. P., 2003, NASA Planet. Data System, EAR-A-I0028-4-SBN0001/SMASSII-V1.0:152_00_TAB
Busarev V. V., Taran M. N., 2002, Proc. of the conf. "Asteroids, Comets, Meteors (ACM 2002)", (ESA-SP-500, November 2002). Technical Univ. Berlin, Berlin, Germany, p. 933
Capaccioni F. et al., 2015, Science, 347, aaa0628
Cochran A. L., Barker E. S., Gray C. L., 2012, Icarus, 218, 144
Cremonese G. et al., 2020, ApJ, 893, L12
Cruikshank D. P. et al., 1998, Icarus, 135, 389
Dlugach J. M., Mishchenko M. I., Mackowski D. W., 2011, J. Quant. Spectrosc. Radiat. Transfer, 112, 1864
Dominik C., 2009, in Henning T., Grün E., Steinacker J., eds, ASP Conf. Ser. Vol. 414, Cosmic Dust—Near and Far. Astron. Soc. Pac., San Francisco, p. 494
Dorschner J., Begemann B., Henning T., Jaeger C., Mutschke H., 1995, A&A, 300, 503
Emde C. et al., 2016, Geosci. Model Dev., 9, 1647
Filacchione G. et al., 2016, Icarus, 274, 334
Fitzsimmons A., Dahlgren M., Lagerkvist C. I., Magnusson P., Williams I. P., 1994, A&A, 282, 684
Fitzsimmons A. et al., 2019, ApJ, 885, L9
Frattin E. et al., 2017, MNRAS, 469, S195
Fulle M., Levasseur-Regourd A. C., McBride N., Hadamcik E., 2000, AJ, 119, 1968
Fulle M. et al. 2020, MNRAS, 493, 4039
Gaffey M. J., Bell J. F., Cruikshank D. P., 1989, in Binzel R. P., Gehrels T., Matthews M. S., eds, Asteroids II. Univ. of Arizona Press, Tucson, p. 98
Gustafson B. Å. S., Kolokolova L., 1999, J. Geophys. Res., 104, 31711
Güttler C. et al., 2019, A&A, 630, A24.
Hanner M. S., Bradley J. P., 2005, in Festou M., Keller H. U., Weaver H. A., eds, Comets II. Univ. Arizona Press, Tucson, p. 555
Hansen J. E., Travis L. D., 1974, Space Sci. Rev., 16, 527
Hiroi T., Zolensky M. E., Pieters C. M., 2001, Science, 293, 2234
Ivlev A. V., Morfill G. E., Konopka U., 2002, Phys. Rev. Lett., 89, 195502
Jewitt D. C., 2002, AJ, 123, 1039
Jewitt D., Luu J., 2019, ApJ, 886, L29
Jewitt D., Hui M. T., Kim Y., Mutchler M., Weave H., Agarwa J., 2020, ApJ, 888, L23
Kimura H., Kolokolova L., Mann I., 2003, A&A, 407, L5
Kolokolova L., Hanner M. S., Levasseur-Regourd A. C., Gustafson B. Å. S., 2004, in Festou M., Keller H. U., Weaver H. A., eds, Comets II. Univ. Arizona Press, Tucson, p. 577
Kolokolova L., Nagdimunov L., Mackowski D., 2018, J. Quant. Spectrosc. Radiat. Trasfer, 204, 138
Kornilov V. et al., 2016a, MNRAS, 462, 4464
Kornilov V. et al., 2016b, Astron. Lett., 42, 616
Kosaza T., Blum J., Okamoto H., Mukai T., 1992, A&A, 263, 423

Kurucz R. L., 2005, Mem. S.A.It. Suppl., 8, 189

Lamy P., Toth I., 2009, Icarus, 201, 674

Lasue J., Levasseur-Regourd A. C., Hadamcik E., Alcouffe G., 2009, Icarus, 199, 129

Liu L., Mishchenko M. I., 2018, Remote Sens., 10, 1634

Lumme K, Penttilä A., 2011, JQSRT, 112, 1658

McCord T. B., Adams J. B., Johnson T. V., 1970, Science, 168, 1445

Mackowski D. W., 1995, Appl. Opt., 34, 3535

Mackowski D. W., Mishchenko M. I., 1996, J. Opt. Soc. Am. A., 13, 2266

Mackowski D. W., Mishchenko M. I., 2011, JQSRT, 112, 2182

Mannel T., Bentley M. S., Schmied R., Jeszenszky H., Levasseur-Regourd A. C., Romstedt J., Torkar K., 2016, MNRAS, 462, S304

McKay A. J., Cochran A. L., Russo N. D., DiSanti M., 2020, ApJ, 889, L10

Mishchenko M. I., Travis L. D., 1997, J. Geophys. Res, 102, 16989

Mishchenko M. I., Travis L. D., Lacis A. A., 2002, Scattering, Absorption, and Emission of Light by Small Particles. Cambridge Univ. Press, Cambridge, UK

Opitom C. et al., 2019, A&A, 631, L8

Petrova E. V., Jockers K., Kiselev N. N., 2000, Icarus, 148, 526

Petrova E. V., Tishkovets V. P., Jockers K., 2004, Sol. Syst. Res., 38, 309

Pizzarello S., Huang Y., Becker L., Poreda R. J., Nieman R. A., Cooper G., Williams M., 2001, Science, 293, 2236

Rotundi A. et al., 2015, Science, 347, aaa3905

Rousseau B. et al., 2018, Icarus, 306, 306

Tenishev V. et al., 2016, MNRAS, 462, S370

Tholen D. J., 1989, in Binzel R. P., Gehrels T., Matthews M. S., eds, Asteroids II. Univ. Arizona Press, Tucson, p. 1139

Tishkovets V. P., Petrova E. V., Jockers K., 2004, JQSRT, 86, 241

Tishkovets V. P., Petrova E. V., 2020, JQSRT, 252, 107116

Vilas F. et al., 1998, NASA Planetary Data System, EAR-A-3-RDR-VILAS-ASTEROID-SPECTRA-V1.1, NASA, USA

Warren S. G., Brandt R. E., 2008, J. Geophys. Res., 113, D14220

West R., Lavvas P., Anderson C., Imanaka H., 2014, in Müller-Wodarg I., Griffith C. A., Lellouch E., Cravens T. E., eds, Titan: Interior, Surface, Atmosphere, and Space Environment. Cambridge Univ. Press, Cambridge, p. 285

Whipple F. L., 1982. In Comets. (A83-13376 03–90) Univ. Arizona Press, Tucson, p. 227

Xing Z., Hanner M., 1997, A&A, 324, 805

Xing Z., Bodewits D., Noonan J., Bannister M. T., 2020, ApJ, 893, L48

Yang B., Kelley M. S. P., Meech K. J., Keane J. V., Protopapa S., Bus S. J., 2020, A&A, 634, L6

Zubko E., Shkuratov Y., Videen G., 2015, JQSRT, 150, 42

This paper has been typeset from a TEX/LATEX file prepared by the author.